Research Square

Preprints are preliminary reports that have not undergone peer review.
They should not be considered conclusive, used to inform clinical practice,
or referenced by the media as validated information.

Assessment of Ecological Environmental Quality and Analysis of Driving Forces in a Plateau–Mountain Region

Sheng Huang
Chengdu University of Information Technology
Jinbao Liu
ljb@cuit.edu.cn

Chengdu University of Information Technology
Xiaorui Qi
Anhui University
Sihan Ni
Chengdu University of Information Technology
Shixiang Zuo
Ecological Protection and Development Research Institute of Aba Tibetan and Qiang Autonomous Prefecture

Article

Keywords: MRSEI, SCS+C, XGBoost–SHAP, PLUS, Ecological environmental quality

Posted Date: September 19th, 2026

DOI: https://doi.org/10.21203/rs.3.rs-10866893/v1

License: This work is licensed under a Creative Commons Attribution 4.0 International License.
Read Full License

Additional Declarations: No competing interests reported.

Assessment of Ecological Environmental Quality and Analysis of Driving Forces in a Plateau–Mountain Region

Sheng Huang[1], Jinbao Liu[1*], Xiaorui Qi[2], Sihan Ni[1], Shixiang Zuo[3]

[1]College of Resources and Environment, Chengdu University of Information Technology, Chengdu, 610225, China.
[2]School of Resources and Environmental Engineering, Anhui University, Hefei, 230601, Anhui, China.
[3]Ecological Protection and Development Research Institute of Aba Tibetan and Qiang Autonomous Prefecture, Wenchuan, 624099, China.

*Corresponding author: ljb@cuit.edu.cn;

ABSTRACT

Topographic illumination effects, NDVI saturation, and inconsistent ecological orientations of annual PCA components can compromise ecological quality assessment in plateau–mountain regions. Based on Landsat observations from 1996 to 2025, this study developed a Modified Remote Sensing Ecological Index (MRSEI) by integrating SCS+C topographic correction, kNDVI, and ecologically direction-constrained PCA. Spatial autocorrelation analysis, XGBoost–SHAP, and PLUS were further employed to investigate spatiotemporal variations in ecological quality, identify driving factors, and project ecological changes to 2034. The results showed that SCS+C substantially reduced terrain-induced illumination effects, and MRSEI exhibited stronger correlations with NPP, EVI, and grazing intensity than the conventional RSEI. Ecological quality generally improved from 1996 to 2025 and showed significant spatial clustering. Topographic, climatic, land-cover, and human-activity factors contributed 30.9%, 27.8%, 23.9%, and 17.4%, respectively. The ecological change prediction model achieved R^2 values above 0.7 in most hindcast periods. Under the natural development scenario, mean regional MRSEI was projected to decrease from 0.6596 in 2024 to 0.6472 in 2034. This framework provides methodological support for long-term ecological monitoring and targeted ecological management in complex mountain regions.

Keywords: MRSEI, SCS+C, XGBoost–SHAP, PLUS, Ecological environmental quality

1 Introduction

Plateau–mountain regions play crucial roles in water conservation and biodiversity maintenance and serve as important ecological security barriers at the regional scale[1,2]. Driven by the combined effects of elevational gradients, topographic relief, and moisture and thermal conditions, mountain vegetation patterns and ecological processes often exhibit pronounced spatial heterogeneity[3,4]. Meanwhile, climate change interacts with human disturbances, including agricultural and pastoral activities, road construction, and tourism development, further increasing the complexity of regional ecosystem dynamics[5]. Therefore, accurately characterizing the spatiotemporal evolution of ecological environmental quality (EEQ) in plateau–mountain regions is essential for ecological conservation and regional sustainable development.

Remote sensing provides broad spatial coverage, repeated observations, and long-term data continuity, making it an important tool for regional ecological monitoring[6]. Early studies generally assessed ecological conditions using individual indicators, such as the normalized difference vegetation index (NDVI), Enhanced Vegetation Index (EVI), leaf area index (LAI), or land surface temperature (LST)[7,8]. However, individual indicators generally capture changes in only one aspect of the environment and cannot comprehensively characterize surface ecological status[9]. The Remote Sensing Ecological Index (RSEI) integrates information on greenness, wetness, dryness, and heat through principal component analysis (PCA) and determines the composite weights of these indicators in a data-driven manner[10]. Consequently, it has been widely applied to ecological quality assessments in urban areas, watersheds, protected

areas, and ecologically fragile regions[11–14]. In recent years, the integration of long-term Landsat time-series data with the Google Earth Engine cloud computing platform has further improved the feasibility and computational efficiency of large-scale, long-term ecological monitoring[15,16]. Despite its comprehensive ecological characterization capacity, RSEI has several limitations in plateau–mountain environments and long-term analyses[17]. Terrain-related variations in slope, aspect, and sun–terrain geometry can introduce radiometric differences between sunlit and shaded slopes, which may propagate into the greenness, wetness, and dryness indicators and bias EEQ estimates[18–20]. NDVI saturation in densely vegetated areas can also weaken the ability of RSEI to differentiate ecological conditions within forests, shrublands, and dense grasslands[21,22]. In addition, the mathematical sign indeterminacy of PCA eigenvectors may reverse the ecological orientation of the first principal component across years, causing positive indicators to contribute negatively and reducing temporal comparability[23]. Although terrain correction, alternative vegetation indices, and PCA direction adjustment have been investigated separately, an integrated framework that simultaneously addresses topographic effects, vegetation-index saturation, and long-term ecological orientation consistency remains limited.

Building on a reliable ecological index, explaining the spatial differentiation of ecological quality and predicting its future changes are essential steps in translating remote sensing observations into actionable information for ecological management[24]. The relationships between ecological quality and topography, climate, land cover, and human activities are often complex and nonlinear. Consequently, conventional linear models may fail to adequately capture threshold effects and potential interactions among these factors[25,26]. Extreme Gradient Boosting (XGBoost) has a strong capacity for modeling nonlinear relationships, whereas SHapley Additive exPlanations (SHAP) can quantify the marginal contribution and direction of influence of each variable on model predictions[27,28]. Their integration therefore provides a useful approach for identifying the major environmental factors associated with the spatial differentiation of ecological quality. However, existing RSEI studies have primarily focused on historical spatiotemporal monitoring, trend analysis, or future assessments based on the continuation of historical patterns[29–31]. Comparatively limited attention has been paid to the extrapolation of dynamic environmental factors, scenario-based land-cover changes, and the propagation of associated uncertainties into ecological quality projections[32–34]. Compared with directly predicting future absolute RSEI values, modeling and predicting RSEI changes at fixed pixel locations enables the integration of baseline ecological conditions, changes in dynamic environmental factors, and land-cover transitions, thereby providing a more explicit modeling pathway for future ecological quality projections.

Aba Tibetan and Qiang Autonomous Prefecture (hereafter referred to as Aba Prefecture), located on the southeastern margin of the Qinghai–Tibet Plateau, is a typical plateau–mountain transition zone characterized by strong topographic relief and ecologically vulnerable high-elevation environments[35]. Using Landsat time-series imagery from 1996 to 2025, this study aimed to: (1) construct a modified remote sensing ecological index (MRSEI) by integrating Sun–Canopy–Sensor plus C (SCS+C) topographic correction, kNDVI, and PCA-based ecological direction constraints, and evaluate its ability to reduce terrain-induced radiometric effects, improve differentiation in densely vegetated areas, and maintain consistent ecological orientation across years; (2) characterize the spatiotemporal variation in ecological quality and quantify the contributions of topographic, climatic, land-cover, and human-related factors using XGBoost–SHAP; and (3) project the spatial distribution of MRSEI in 2034 under a natural development scenario by coupling dynamic driver extrapolation, PLUS-based land-cover simulation, and an XGBoost ecological change model. This study establishes an integrated framework for ecological index construction, driver interpretation, and future projection, providing methodological support for ecological monitoring and conservation in plateau–mountain regions.

2 Regional Setting

Aba Tibetan and Qiang Autonomous Prefecture (hereafter referred to as Aba Prefecture; 30°35′–34°19′ N, 100°31′–104°27′ E) is located in northwestern Sichuan Province on the eastern margin of the Qinghai–Tibet Plateau. It covers approximately 84,242 km^2 and forms a representative ecological transition zone between the Qinghai–Tibet Plateau and the Sichuan Basin (Figure 1a). The region plays an important role in water regulation, soil conservation, and regional ecological security. Aba Prefecture is characterized by pronounced topographic relief, with elevations ranging from 764 to 5973 m (Figure 1b). The northwestern part is dominated by high plateaus, the central part by mountainous terrain, and the southeastern part by deeply incised alpine valleys. Strong elevational gradients and associated hydrothermal variation result in marked vertical differentiation in climate, vegetation, and ecological processes. The long-term mean annual temperature and precipitation are approximately 9 °C and 665 mm, respectively, but vary considerably across elevation zones and topographic units[36]. Grassland and forest are the dominant land-cover types, occurring mainly in the eastern and southeastern mountains and valleys,

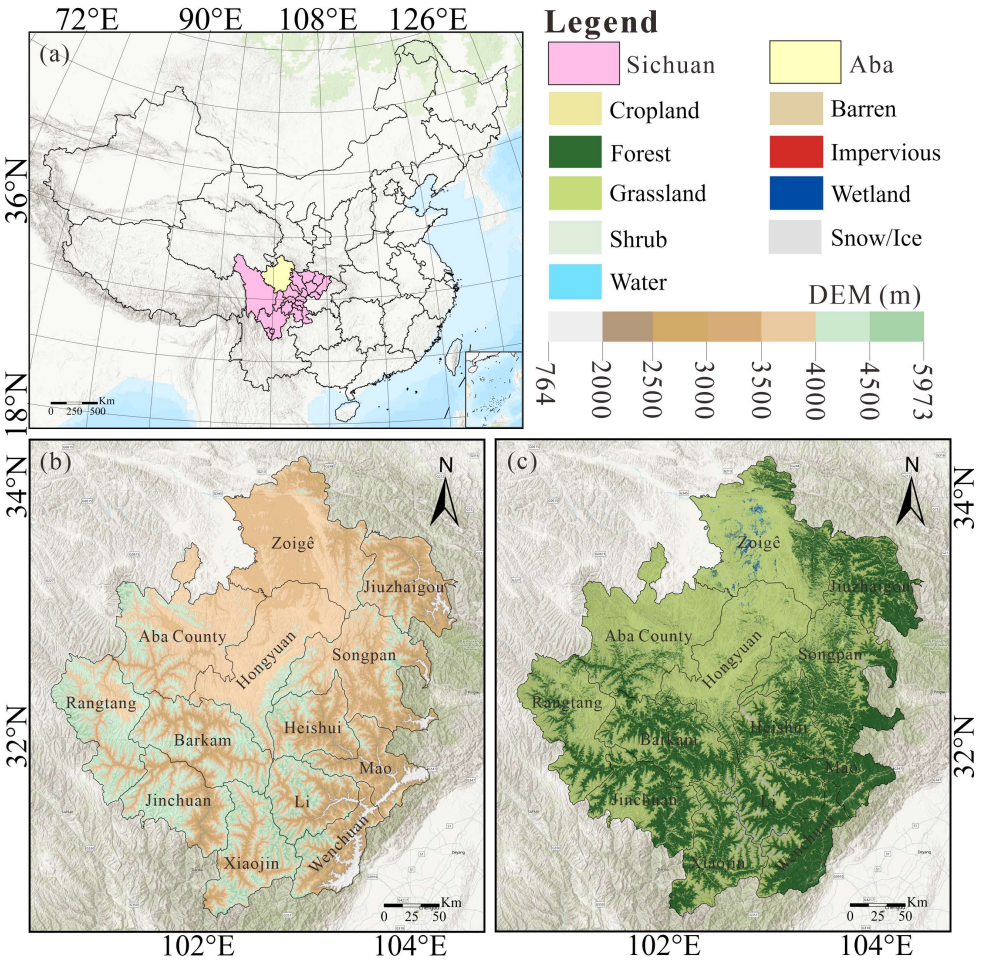


Fig. 1. Location and geographical characteristics of Aba Prefecture. (**a**) Location of Aba Prefecture in Sichuan Province, China. (**b**) Topographic characteristics of Aba Prefecture. (**c**) Land-cover distribution in Aba Prefecture.

whereas barren land, snow, and ice are concentrated at higher elevations. Built-up land occupies only a small proportion of the region and is mainly distributed in county seats and river valleys (Figure 1c). Although ecological restoration programs have promoted regional recovery, ecosystems remain vulnerable to the combined effects of high-elevation climatic constraints and human disturbances associated with tourism and agricultural and pastoral activities [37–39].

3 Materials and Methods

3.1 Data Sources and Preprocessing

This study integrated multi-source datasets for Aba Prefecture from 1996 to 2025, including remote sensing imagery, topographic, climatic, land-cover, and socioeconomic data (Table 1). The remote sensing imagery was acquired from the Google Earth Engine platform and subjected to radiometric and atmospheric corrections, as well as cloud, cloud-shadow, and snow masking. To minimize seasonal differences, valid images acquired between 1 June and 30 September of each year were selected. To prevent water pixels from affecting the normalization of ecological indicators and the PCA loadings, permanent water bodies were identified using the annual water classification product from the JRC Global Surface Water dataset and masked before the ecological indicators were calculated [40]. Because the parameters used for topographic correction vary with solar geometry and image acquisition time, SCS+C topographic correction was applied separately to the optical bands of each valid scene [41]. The corrected images acquired within the same year were then median-composited to generate annual surface reflectance composites. Finally, all datasets were standardized to a common coordinate reference system, spatial extent, and pixel grid, and annual time series of all variables were constructed at fixed pixel locations to ensure spatial correspondence across years.

Table 1. Sources of the datasets used in this study.

Dataset	Temporal coverage (years)	Spatial resolution (m)	Database URL
Landsat 5 TM	1996–2011	30	https://www.usgs.gov/
Landsat 7 ETM+	2012	30	https://www.usgs.gov/
Landsat 8 OLI/TIRS	2013–2025	30	https://www.usgs.gov/
Meteorological data	1996–2024	1000	https://cms.casdc.cn/
China Land Cover Dataset (CLCD)	1996–2025	30	https://doi.org/10.5281/zenodo.18180184
Net primary productivity (NPP)	1986–2024	500	https://www.gisrs.cn/?data_113/33d94526-9264-440f-8f4a-23fcde74c512.html
Enhanced Vegetation Index (EVI)	2000–2020	250	https://doi.org/10.5281/zenodo.7979989
Defense Meteorological Satellite Program (DMSP) nighttime light	1996–2024	1000	https://doi.org/10.12041/geodata.54416522887785.ver2.db
Population density (PD)	1996–2024	1000	https://doi.org/10.48690/lsm/zew2-1n91
Fractional Vegetation Cover (FVC)	2000–2024	250	https://doi.org/10.11888/Terre.tpdc.300330
Long-term High-resolution Grazing Intensity (LHGI)	1996–2024	1000	https://doi.org/10.6084/m9.figshare.26195684.v3

3.2 Methods

3.2.1 SCS+C Topographic Correction

SCS+C topographic correction was applied to the optical bands of each Landsat scene[42]. First, the terrain slope β and aspect ϕ_a were derived from the Digital Elevation Model (DEM). These parameters were then combined with the solar zenith angle θ_s and solar azimuth angle ϕ_s at the image acquisition time to calculate the pixel-scale solar incidence angle i:

$$\cos i = \cos\theta_s \cos\beta + \sin\theta_s \sin\beta \cos\left(\phi_s - \phi_a\right). \tag{1}$$

For each optical band λ of each scene, a linear regression relationship was established between the original surface reflectance and $\cos i$. The corresponding band-specific parameter C_λ was then calculated from the regression slope and intercept:

$$\rho_\lambda = a_\lambda \cos i + b_\lambda, \tag{2}$$

$$C_\lambda = \frac{b_\lambda}{a_\lambda}. \tag{3}$$

where ρ_λ denotes the original surface reflectance of band λ; a_λ and b_λ are the slope and intercept, respectively, of the linear regression equation for band λ; and C_λ is the empirical correction parameter for the corresponding band.

The topographically corrected surface reflectance, $\rho_{\mathrm{tc},\lambda}$, was subsequently calculated using the SCS+C model:

$$\rho_{\mathrm{tc},\lambda} = \rho_\lambda \frac{\cos\theta_s \cos\beta + C_\lambda}{\cos i + C_\lambda}. \tag{4}$$

The inclusion of the C_λ parameter in the SCS+C model reduces the risk of overcorrection under low-illumination terrain conditions. After topographic correction, the corrected optical bands were used to calculate the kNDVI, WET, and NDBSI ecological indicators.

3.2.2 Construction of the MRSEI

The conventional Remote Sensing Ecological Index (RSEI) integrates the normalized difference vegetation index (NDVI), wetness component (WET), land surface temperature (LST), and normalized difference built-up and soil index (NDBSI) to represent greenness, wetness, heat, and dryness, respectively. In this study, NDVI was replaced with the kernel normalized difference vegetation index (kNDVI) to improve the differentiation of densely vegetated areas, whereas WET, LST, and NDBSI were retained. The four indicators were calculated on the Google Earth Engine platform and normalized to the range of $[0, 1]$ before principal component analysis (PCA) was performed (Table 2).

When PCA is performed independently for each year, the eigenvector and component scores associated with PC1 are subject to global sign indeterminacy, which may reverse the ecological interpretation

Table 2. Summary of the calculation methods for the remote sensing ecological indicators and the composite index.

Index	Ecological dimension	Formula	Reference
kNDVI	Greenness	$\mathrm{kNDVI} = \tanh\left(\mathrm{NDVI}^2\right),$ $\mathrm{NDVI} = \frac{\rho_{\mathrm{NIR}} - \rho_{\mathrm{Red}}}{\rho_{\mathrm{NIR}} + \rho_{\mathrm{Red}}}$	[22,43]
WET	Wetness	$\mathrm{WET}_{L5} = 0.0315\rho_{\mathrm{Blue}} + 0.2021\rho_{\mathrm{Green}} + 0.3102\rho_{\mathrm{Red}} + 0.1594\rho_{\mathrm{NIR}} - 0.6806\rho_{\mathrm{SWIR1}} - 0.6109\rho_{\mathrm{SWIR2}},$ $\mathrm{WET}_{L7} = 0.2626\rho_{\mathrm{Blue}} + 0.2141\rho_{\mathrm{Green}} + 0.0926\rho_{\mathrm{Red}} + 0.0656\rho_{\mathrm{NIR}} - 0.7629\rho_{\mathrm{SWIR1}} - 0.5388\rho_{\mathrm{SWIR2}},$ $\mathrm{WET}_{L8} = 0.1511\rho_{\mathrm{Blue}} + 0.1973\rho_{\mathrm{Green}} + 0.3283\rho_{\mathrm{Red}} + 0.3407\rho_{\mathrm{NIR}} - 0.7117\rho_{\mathrm{SWIR1}} - 0.4559\rho_{\mathrm{SWIR2}}$	[44–46]
LST	Heat	$\mathrm{LST} = \mathrm{ST}_K - 273.15$	[47,48]
NDBSI	Dryness	$\mathrm{IBI} = \frac{\frac{2\rho_{\mathrm{SWIR1}}}{\rho_{\mathrm{SWIR1}}+\rho_{\mathrm{NIR}}} - \left(\frac{\rho_{\mathrm{NIR}}}{\rho_{\mathrm{NIR}}+\rho_{\mathrm{Red}}} + \frac{\rho_{\mathrm{Green}}}{\rho_{\mathrm{Green}}+\rho_{\mathrm{SWIR1}}}\right)}{\frac{2\rho_{\mathrm{SWIR1}}}{\rho_{\mathrm{SWIR1}}+\rho_{\mathrm{NIR}}} + \left(\frac{\rho_{\mathrm{NIR}}}{\rho_{\mathrm{NIR}}+\rho_{\mathrm{Red}}} + \frac{\rho_{\mathrm{Green}}}{\rho_{\mathrm{Green}}+\rho_{\mathrm{SWIR1}}}\right)}$ $\mathrm{SI} = \frac{(\rho_{\mathrm{SWIR1}} + \rho_{\mathrm{Red}}) - (\rho_{\mathrm{NIR}} + \rho_{\mathrm{Blue}})}{(\rho_{\mathrm{SWIR1}} + \rho_{\mathrm{Red}}) + (\rho_{\mathrm{NIR}} + \rho_{\mathrm{Blue}})}$ $\mathrm{NDBSI} = \frac{\mathrm{IBI} + \mathrm{SI}}{2}$	[10,49,50]
MRSEI	Composite index	$\mathrm{MRSEI} = \mathrm{PCA}\left(\mathrm{kNDVI}, \mathrm{WET}, \mathrm{LST}, \mathrm{NDBSI}\right),$ $V_{\mathrm{kNDVI,WET}} > 0, \quad V_{\mathrm{LST,NDBSI}} < 0$	[51]

of PC1 across years (Figure 2b and e). Building on the ecological direction-constraint concept proposed by Ning et al.[52], this study used the absolute magnitudes of the annual PC1 loadings as data-driven weights and imposed predefined ecological directions on the four indicators. Specifically, kNDVI and WET were assigned positive directions because they represent favorable ecological conditions, whereas LST and NDBSI were assigned negative directions because they represent thermal and dryness-related ecological stress (Figure 2c and g). The direction-adjusted, loading-weighted indicators were then combined to reconstruct an ecologically directed composite score. For ecological quality classification, the annually normalized MRSEI values were divided into five equal-width classes following Xu et al.[53]: poor [0, 0.2], fair (0.2, 0.4], moderate (0.4, 0.6], good (0.6, 0.8], and excellent (0.8, 1.0]. A class-transition matrix was subsequently constructed to characterize changes among ecological quality classes during the study period.

3.3 Spatial Autocorrelation Analysis

Global Moran's I was used to quantify the overall spatial autocorrelation of EEQ, while local Moran's I, or local indicators of spatial association (LISA), was applied to identify local clusters and spatial outliers[54]. Global Moran's I ranges from -1 to 1 and is calculated as follows:

$$I = \frac{n}{S_0} \frac{\sum_{i=1}^{n}\sum_{j=1}^{n} w_{ij}\left(y_i - \bar{y}\right)\left(y_j - \bar{y}\right)}{\sum_{i=1}^{n}\left(y_i - \bar{y}\right)^2}, \qquad S_0 = \sum_{i=1}^{n}\sum_{j=1}^{n} w_{ij}. \tag{5}$$

where w_{ij} denotes the spatial weight between spatial units i and j; y_i and y_j are the MRSEI values of spatial units i and j, respectively; n is the total number of spatial units; $\bar{y}$ is the mean MRSEI value; and S_0 is the sum of all spatial weights.

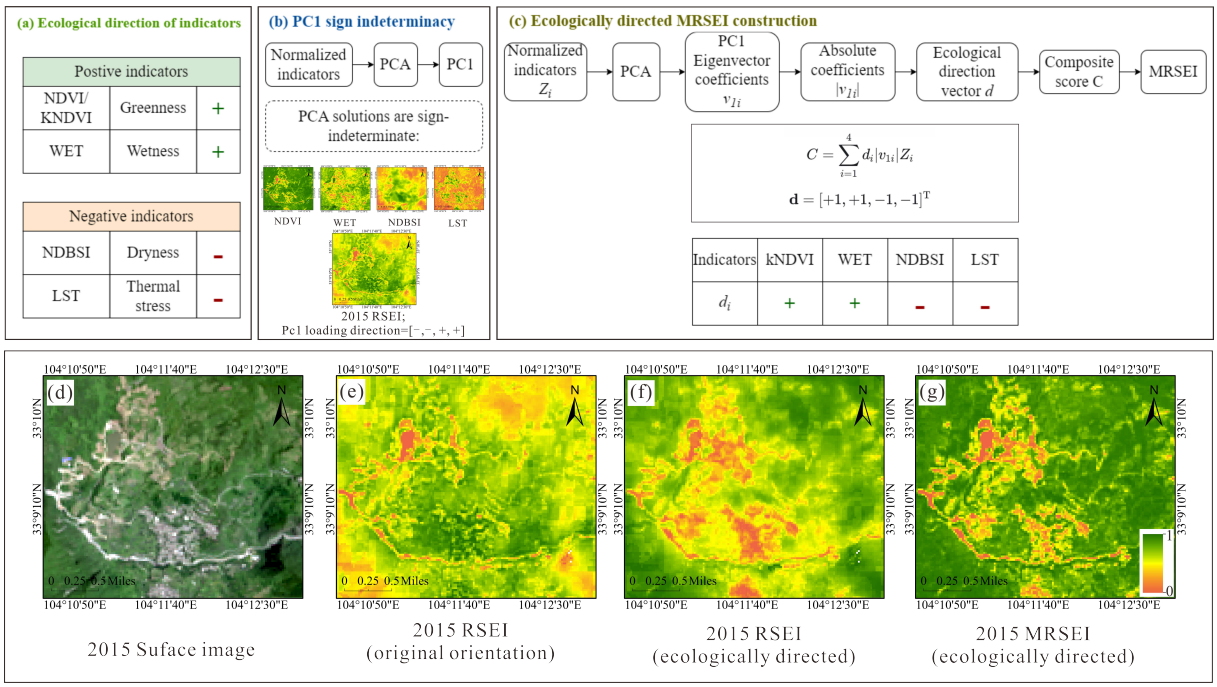


Fig. 2. Construction process of the MRSEI. (**a**) Predefined ecological directions of the input indicators. (**b**) PC1 sign indeterminacy and differences in loading direction. (**c**) Workflow for constructing an ecologically directed MRSEI. (**d**) Landsat surface reflectance image in 2015. (**e**) 2015 RSEI with an original PC1 orientation. (**f**) 2015 RSEI with a constrained PC1 orientation. (**g**) 2015 MRSEI with a constrained PC1 orientation.

Local Moran's I_i, a local indicator of spatial association, quantifies spatial association at individual locations and thereby identifies local spatial clusters and spatial outliers [55]. It was calculated as follows:

$$I_i = \frac{y_i - \bar{y}}{\frac{1}{n}\sum_{k=1}^{n}(y_k - \bar{y})^2} \sum_{\substack{j=1 \\ j \neq i}}^{n} w_{ij}\,(y_j - \bar{y})\,. \tag{6}$$

where I_i is the local Moran's I statistic for spatial unit i; y_i and y_j denote the MRSEI values of spatial unit i and its neighboring spatial unit j, respectively; $\bar{y}$ is the mean MRSEI value; w_{ij} is an element of the spatial weight matrix; and n is the total number of spatial units.

3.4 XGBoost–SHAP Model

An XGBoost–SHAP framework was used to model and interpret the spatial differentiation of ecological quality, with MRSEI as the response variable and topographic, climatic, land-cover, and human-activity factors as predictors [56]. Following the chronological sequence, samples from 1996–2019 were used for model training, whereas those from 2020–2024 were retained as an independent validation set. Model hyperparameters were optimized using randomized search with five-fold GroupKFold cross-validation, in which year was used as the grouping variable to reduce information leakage between samples from the same year. Model performance was evaluated using the coefficient of determination (R^2), root mean square error (RMSE), and mean absolute error (MAE).

SHAP values were calculated from the optimal XGBoost model to quantify the contribution and direction of influence of each predictor. Each model prediction was decomposed into a baseline value and the marginal contributions of individual factors. The SHAP decomposition was expressed as follows:

$$f(\mathbf{x}_s) = \phi_0 + \sum_{j=1}^{M} \phi_{s,j}. \tag{7}$$

where $f(\mathbf{x}_s)$ denotes the MRSEI value predicted by the XGBoost model for sample s; ϕ_0 is the baseline prediction of the model; M is the number of input driving factors; and $\phi_{s,j}$ is the SHAP value of feature j for sample s, representing its contribution to the predicted MRSEI value.

Because higher MRSEI values represent better ecological quality, positive SHAP values indicate that a predictor increases the predicted MRSEI relative to the model's baseline prediction, whereas negative SHAP values indicate that it decreases the predicted MRSEI. The absolute SHAP value represents the

magnitude of the predictor's contribution to an individual prediction, and the mean absolute SHAP value across all samples was used to quantify global predictor importance.

3.5 Future Ecological Quality Projection

This study developed an ecological quality projection framework integrating dynamic-driver extrapolation, PLUS-based land-cover scenario simulation, and an XGBoost ecological change model. Ten-year sample pairs were constructed at fixed pixel locations using the historical time series from 1996 to 2024. Rather than directly predicting future MRSEI values, the model predicted the decadal change in MRSEI:

$$\Delta\mathrm{MRSEI}_{t,t+10} = \mathrm{MRSEI}_{t+10} - \mathrm{MRSEI}_{t}. \tag{8}$$

where $\Delta\mathrm{MRSEI}_{t,t+10}$ denotes the change in MRSEI from year t to year $t+10$; MRSEI_t is the MRSEI value in the initial year; and MRSEI_{t+10} is the corresponding value ten years later.

The predictors included baseline MRSEI, baseline values and decadal changes in the dynamic environmental factors, static topographic factors, and land-cover transition information. Sample pairs with target years no later than 2014 were used for model training, whereas the 2014–2024 pair was retained as a temporally held-out historical hindcast. Hyperparameters were optimized using grouped cross-validation, with the target year used as the grouping variable. The final model contained 500 trees, with a maximum depth of 3, a learning rate of 0.1, a subsampling ratio of 0.9, and a feature-subsampling ratio of 0.7. Hindcast performance was evaluated using R^2, RMSE, MAE, Bias, and the spatial distribution of residuals.

Future dynamic drivers were generated separately for each variable. Candidate extrapolation methods were evaluated through rolling-origin historical hindcasting, in which only observations available before each target year were used to generate predictions.

Future land-cover patterns were simulated using the Patch-generating Land Use Simulation (PLUS) model[57]. For historical validation, observed land cover in 2014 was used as the baseline to simulate the 2024 pattern, which was compared with the observed 2024 land cover using overall accuracy, the Kappa coefficient, and the figure of merit. For future projection, the observed 2024 land cover was used as the baseline, and the 2034 land-cover demand under the natural development scenario was spatially allocated using the LEAS and CARS modules. To assess the sensitivity of predicted ecological quality to errors in simulated land-cover inputs, we conducted an ecological hindcast from 2014 to 2024 using two alternative land-cover maps for 2024: the observed map and a simulated map produced by a two-stage XGBoost transition model coupled with demand-constrained spatial allocation. Differences between the resulting ecological-quality predictions were used to quantify the influence of land-cover simulation errors.

After completion of the temporal hindcast, the 2014–2024 sample pair was incorporated into the final training dataset. Using the observed ecological and environmental conditions in 2024 as the baseline, the decadal MRSEI change for 2024–2034 was predicted as:

$$\begin{aligned}\Delta\mathrm{MRSEI}^{\mathrm{pred}}_{2024,2034} = f\big(&\mathrm{MRSEI}_{2024}, \mathbf{X}_{2024}, \Delta\mathbf{X}^{\mathrm{pred}}_{2024,2034}, \mathbf{T},\\ &\mathrm{LC}_{2024}, \mathrm{LC}^{\mathrm{PLUS}}_{2034}\big).\end{aligned} \tag{9}$$

where the superscript "pred" identifies model-predicted quantities; $\mathbf{X}_{2024}$ denotes the dynamic driving factors in 2024; $\Delta\mathbf{X}^{\mathrm{pred}}_{2024,2034}$ represents the predicted changes in the dynamic driving factors from 2024 to 2034; $\mathbf{T}$ denotes the topographic factors; LC_{2024} is the observed land cover in 2024; and $\mathrm{LC}^{\mathrm{PLUS}}_{2034}$ represents the land cover under the 2034 natural development scenario simulated using the PLUS model. The function $f(\cdot)$ denotes the trained XGBoost prediction model.

Finally, the predicted decadal change was added to the observed MRSEI in 2024 to reconstruct the ecological quality in 2034:

$$\mathrm{MRSEI}^{\mathrm{pred}}_{2034} = \mathrm{clip}\left(\mathrm{MRSEI}_{2024} + \alpha\,\Delta\mathrm{MRSEI}^{\mathrm{pred}}_{2024,2034},\, 0,\, 1\right). \tag{10}$$

where $\mathrm{clip}(\cdot)$ constrains the predicted values to the theoretical MRSEI range $[0, 1]$; and α is a change-shrinkage coefficient determined through historical hindcasting. In this study, α was set to 1.0.

4 Results

4.1 Topographic Correction and MRSEI Model Stability

Aba Prefecture is characterized by pronounced topographic relief. To evaluate the extent to which SCS+C correction reduced terrain-induced illumination effects, the relationships between surface

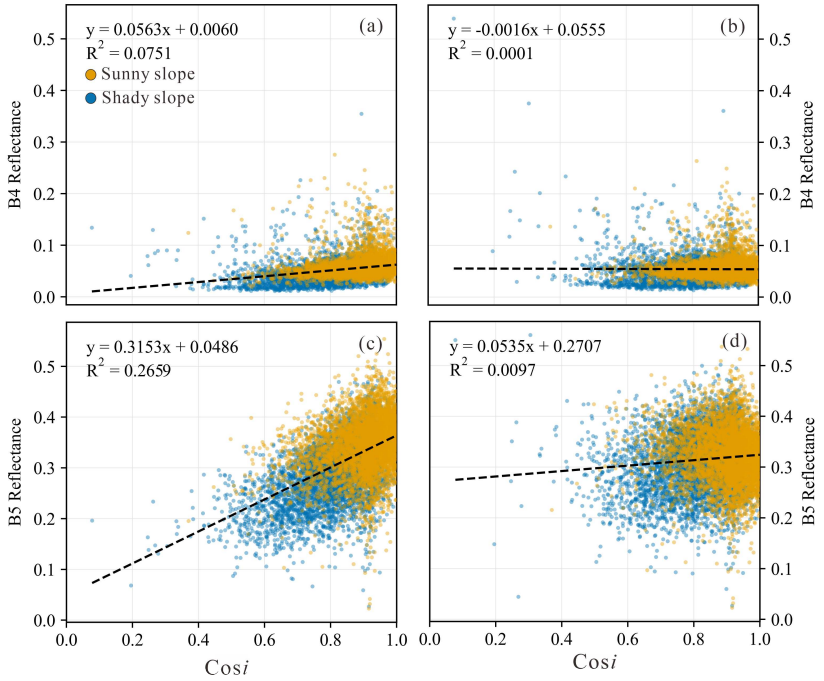


Fig. 3. Relationships between surface reflectance and the cosine of the solar incidence angle ($\cos i$) before and after SCS+C topographic correction: red band before (**a**) and after (**b**) correction, and near-infrared band before (**c**) and after (**d**) correction. Sun-facing and shaded slopes were defined by aspect ranges of 135°–225° and 0°–45° or 315°–360°, respectively.

reflectance in the red (B4) and near-infrared (B5) bands and the cosine of the solar incidence angle $\cos i$ were compared before and after correction (Figure 3). Before correction, the reflectance of both B4 and B5 increased with increasing $\cos i$. This relationship was more pronounced for B5, with a regression slope of 0.3153 and an R^2 of 0.2659, both exceeding the corresponding values of 0.0563 and 0.0751 for B4 (Figure 3a and c). After SCS+C correction, the linear relationships between surface reflectance and $\cos i$ were substantially weakened for both bands. For B4, the regression slope decreased to −0.0016 and R^2 decreased to 0.0001; for B5, the regression slope decreased to 0.0535 and R^2 decreased to 0.0097 (Figure 3b and d). After correction, the regression lines became substantially flatter, and the linear relationship between B4 reflectance and $\cos i$ approached zero.

In addition, NPP, EVI, and LHGI were selected as external ecological reference indicators to further evaluate the ability of MRSEI to characterize changes in regional ecological environmental quality. Pearson's correlation coefficient (r) and Spearman's rank correlation coefficient (ρ) were calculated between these indicators and both MRSEI and the conventional RSEI (Table 3). The results showed that MRSEI was positively correlated with NPP and EVI but negatively correlated with LHGI, consistent with ecological expectations. Specifically, Pearson's r and Spearman's ρ between MRSEI and NPP were 0.57 and 0.59, respectively, exceeding the corresponding values of 0.38 and 0.42 for RSEI. The corresponding coefficients between MRSEI and EVI were 0.61 and 0.51, respectively, which were also higher than those for RSEI (0.38 and 0.31). For LHGI, MRSEI yielded Pearson's $r = -0.49$ and Spearman's $\rho = -0.51$, respectively; their absolute magnitudes were greater than the corresponding values for RSEI ($r = -0.33$ and $\rho = -0.40$, respectively). Overall, MRSEI exhibited stronger correlations with all three external ecological reference indicators than the conventional RSEI, demonstrating greater consistency with variations in vegetation productivity, vegetation growth conditions, and grazing pressure within the study area.

Table 3. Correlations of MRSEI and RSEI with ecological reference indicators.

Indicator	MRSEI		RSEI	
	Pearson's r	Spearman's ρ	Pearson's r	Spearman's ρ
NPP	0.57	0.59	0.38	0.42
EVI	0.61	0.51	0.38	0.31
LHGI	−0.49	−0.51	−0.33	−0.40

Note: NPP, net primary productivity; EVI, Enhanced Vegetation Index; LHGI, long-term high-resolution grazing intensity.

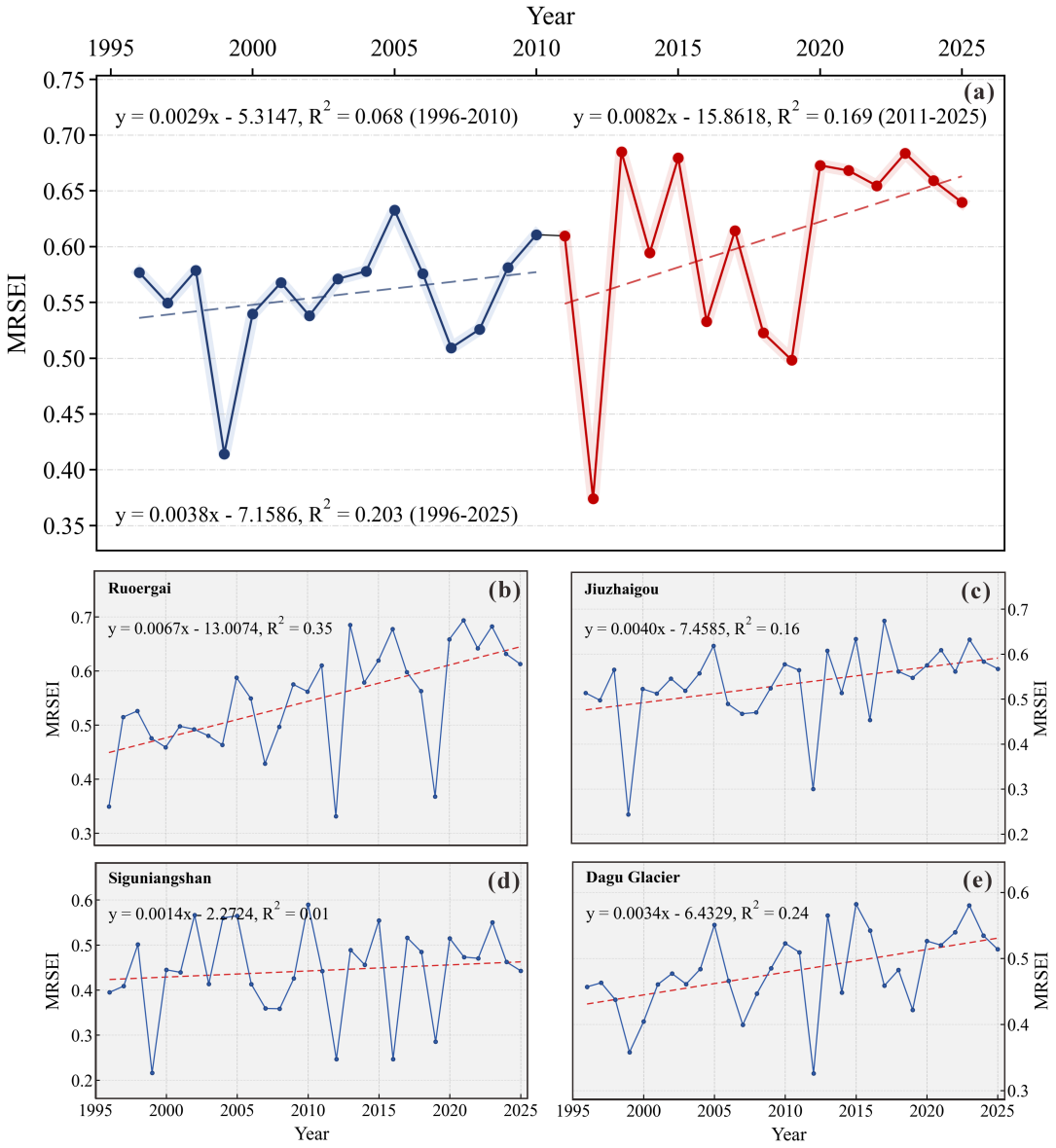


Fig. 4. Temporal trends in MRSEI from 1996 to 2025. (**a**) Temporal trends in MRSEI from 1996 to 2025 in Aba Prefecture. (**b**) Temporal trends in MRSEI from 1996 to 2025 in Ruoergai Nature Reserve. (**c**) Temporal trends in MRSEI from 1996 to 2025 in Jiuzhaigou Nature Reserve. (**d**) Temporal trends in MRSEI from 1996 to 2025 in Siguniangshan Nature Reserve. (**e**) Temporal trends in MRSEI from 1996 to 2025 in Dagu Glacier Nature Reserve.

4.2 Spatiotemporal Variations in Ecological Environmental Quality

From 1996 to 2025, MRSEI in Aba Prefecture exhibited an overall fluctuating upward trend (Figure 4a). The linear regression slope for the entire study period was 0.0038, with an R^2 of 0.203. During 1996–2010, the fitted slope was 0.0029 and R^2 was 0.068; during 2011–2025, the slope increased to 0.0082, with an R^2 of 0.169. Thus, the rate of increase was higher in the latter period than in the former. The time-series results revealed pronounced decreases in MRSEI in 1999 and 2012, when the values were lower than those in the adjacent years. After 2018, MRSEI remained at relatively high levels in most years, particularly during 2020–2024. However, it declined slightly in 2025 compared with the preceding high-value years. At the long-term scale, EEQ in Aba Prefecture exhibited an overall tendency toward improvement, although substantial interannual fluctuations remained.

The temporal variations in MRSEI also differed among the representative nature reserves (Figure 4b–e). The Ruoergai Nature Reserve exhibited the highest fitted slope of 0.0067, with an R^2 of 0.35, although several low-value years remained evident in the time series (Figure 4b). The fitted slope of MRSEI in the Jiuzhaigou Nature Reserve was 0.0040, with an R^2 of 0.16 (Figure 4c). The Siguniangshan Nature Reserve exhibited the lowest fitted slope of only 0.0014, with an R^2 of 0.01 (Figure 4d). In the Dagu Glacier Nature Reserve, the fitted slope was 0.0034, with an R^2 of 0.24, indicating a fluctuating upward trend in ecological quality (Figure 4e).

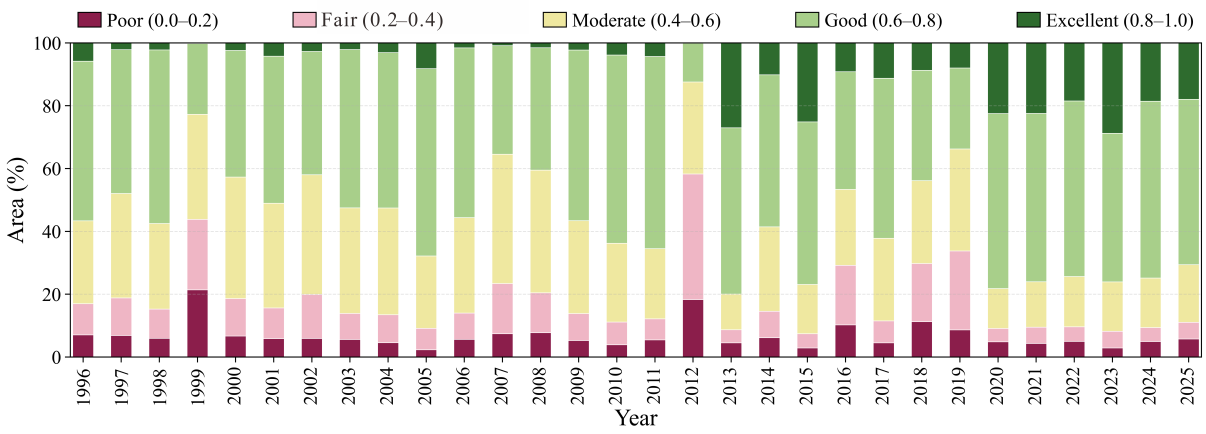


Fig. 5. Changes in the area proportions of different EEQ classes in Aba Prefecture from 1996 to 2025.

The interannual changes in the composition of ecological quality in Aba Prefecture were further quantified by the area proportions of the five EEQ classes (Figure 5). Except for several years with relatively low ecological quality, the poor and fair classes generally accounted for small proportions, whereas the good class was dominant in most years. From 1996 to 2011, the moderate and good classes jointly dominated the EEQ pattern in Aba Prefecture. After 2013, the combined proportion of the good and excellent classes increased markedly. In particular, these two classes exhibited a pronounced proportional advantage in 2015, 2020, and 2021–2024.

4.3 Spatial Autocorrelation Patterns of Ecological Environmental Quality

Spatial autocorrelation analysis was conducted using the multiyear mean MRSEI to characterize the spatial clustering patterns of EEQ in Aba Prefecture. The global Moran's I was 0.89, indicating strong spatial clustering of similar MRSEI values across Aba Prefecture (Figure 6). The LISA cluster results showed that areas failing to pass the significance test accounted for 63.77% of the valid assessment area. Among the statistically significant clusters, the High–High and Low–Low types were dominant, accounting for 23.29% and 12.87%, respectively. The High–High clusters were primarily distributed in the eastern and southeastern parts of the study area, with continuous distributions also observed in some south-central areas. The Low–Low clusters were concentrated mainly in the western, central, and parts of the northern regions, generally exhibiting banded or patchy spatial patterns. The Low–High and High–Low spatial outlier types accounted for only 0.05% and 0.02%, respectively, and both exhibited scattered distributions.

In addition, the spatial relationships within the four representative nature reserves showed that relatively continuous High–High clusters occurred within and around the Jiuzhaigou and Siguniangshan nature reserves. The Ruoergai Nature Reserve was dominated by areas that did not pass the significance test, while both Low–Low and High–High clusters occurred in its surrounding areas. Within and around the Dagu Glacier Nature Reserve, nonsignificant areas were interspersed with localized cluster types.

4.4 Driving Factors of Ecological Environmental Quality

Before conducting the SHAP analysis, the fitting performance and generalization ability of the XGBoost model were evaluated. The model was trained using samples from 1996–2019 and independently validated using samples from 2020–2024. The R^2, RMSE, and MAE values were 0.71, 0.13, and 0.098 for the training set and 0.44, 0.19, and 0.155 for the validation set, respectively.

The SHAP analysis revealed substantial differences in the contributions of environmental factors to the MRSEI (Figure 7). Land-cover type (CLCD) made the largest contribution, accounting for 23.9% of the total mean absolute SHAP value, followed by elevation (DEM, 19.1%), temperature (14.7%), precipitation (13.1%), and grazing intensity (LHGI, 12.2%). Aspect, slope, and population density made relatively small contributions of 6.8%, 5.0%, and 5.0%, respectively. Nighttime light contributed only 0.2%, indicating limited explanatory power. Overall, the spatial variation in ecological environmental quality across Aba Prefecture was primarily controlled by topographic and climatic conditions, with land cover also playing an important role, whereas anthropogenic factors made a relatively limited overall contribution.

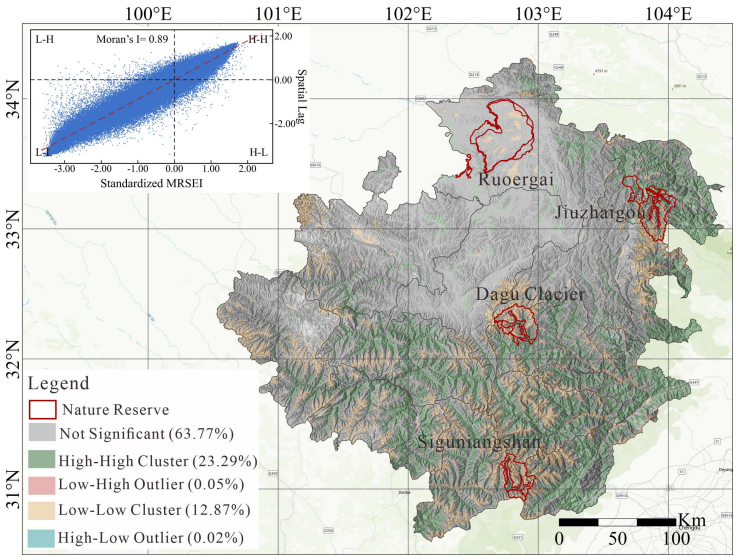


Fig. 6. Spatial autocorrelation and LISA cluster patterns of MRSEI in Aba Prefecture.

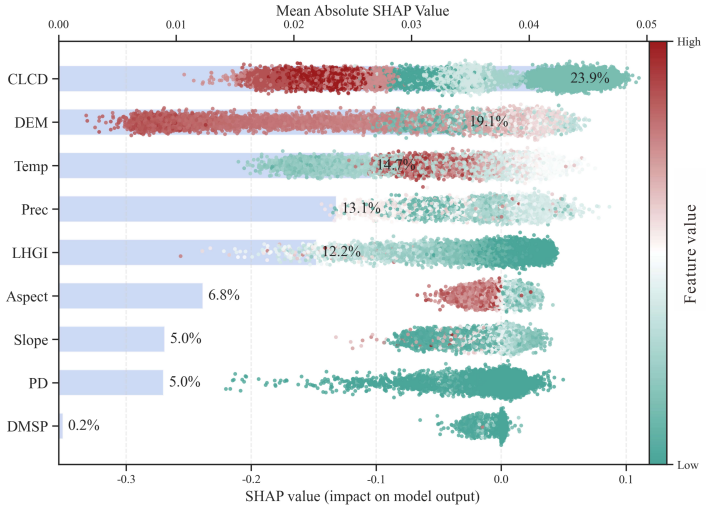


Fig. 7. Contributions of the environmental factors to MRSEI.

4.5 Future Ecological Environmental Quality

Using the 2014 land-cover data as the baseline, the PLUS model incorporated climatic, topographic, socioeconomic, and distance-related driving factors to hindcast the land-cover pattern in 2024, which was then compared with the observed CLCD data. The results showed an overall accuracy of 0.96 and a Kappa coefficient of 0.92. However, only approximately 3.5% of the pixels in the study area underwent land-cover changes between 2014 and 2024, resulting in an FoM of 0.03. Based on these results, the land-cover demand for each class in 2034 was projected according to the land-cover transition patterns observed during 2014–2024. Spatial allocation was then performed using the CARS module to generate the 2034 land-cover pattern under the natural development scenario (Figure 8a).

Table 4. Construction methods for the variables used in the 2034 MRSEI projection.

Variable	Data period	Construction method
Temp	1996–2024	Pixel-wise OLS extrapolation to 2034
Prec	2015–2024	Pixel-wise median of 2015–2024 values
PD	2024	Persistence assumption (2034 = 2024)
LHGI	2024	Persistence assumption (2034 = 2024)
DMSP	2024	Persistence assumption (2034 = 2024)
CLCD	2024 and 2034	PLUS-simulated 2034 natural development scenario

Following the independent hindcast validation summarized in Table 5, the 2014–2024 sample pairs were incorporated into the training dataset, and the final XGBoost model was refitted using all available

Table 5. Temporal hindcast performance of the XGBoost model for predicting decadal changes in MRSEI.

Hindcast period	R^2	RMSE	MAE	Bias
1999–2009	0.440	0.158	0.125	−0.083
2000–2010	0.712	0.121	0.092	−0.003
2001–2011	0.760	0.114	0.087	−0.009
2003–2013	0.765	0.126	0.101	−0.042
2004–2014	0.687	0.133	0.099	0.035
2014–2024	**0.707**	**0.135**	**0.101**	**−0.046**

Note: The 2014–2024 period was used as a temporally independent holdout hindcast. Bias was calculated as the mean difference between predicted and observed changes in MRSEI; negative values indicate underestimation.

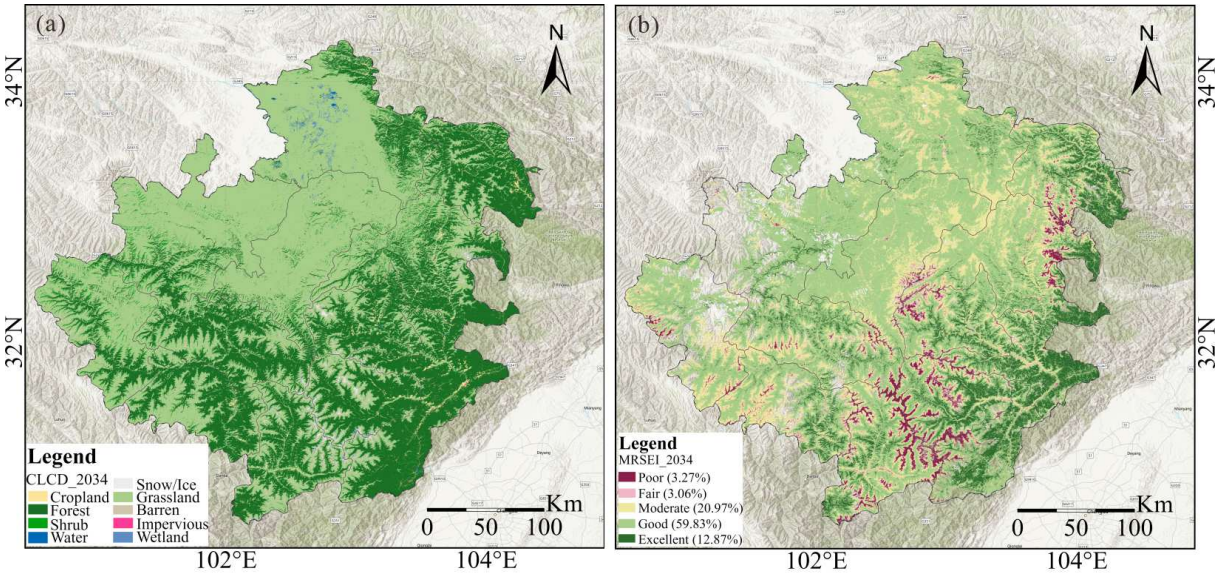


Fig. 8. Ecological projections for 2034. (**a**) Projected land-cover distribution in Aba Prefecture in 2034. (**b**) Spatial distribution of MRSEI in 2034.

historical samples. The predictor variables for the 2034 projection were then generated using the variable-specific construction methods summarized in Table 4. The PLUS-simulated land cover for 2034 and the projected future environmental factors were then used to estimate MRSEI in 2034 (Figure 8b). Under the natural development scenario, the mean MRSEI of Aba Prefecture decreased from 0.6596 in 2024 to 0.6472 in 2034, corresponding to a regional mean decrease of 0.0124. The five-class ecological quality statistics showed that the proportions of areas classified as poor, fair, moderate, good, and excellent in 2024 were 4.94%, 4.43%, 15.72%, 56.34%, and 18.57%, respectively. By 2034, these proportions were projected to change to 3.27%, 3.06%, 20.97%, 59.83%, and 12.87% (Figure 8b), respectively. The proportion of the excellent class decreased by 5.7 percentage points. The proportion of the moderate and good classes increased by 5.25 percentage points and 3.49 percentage points, respectively. The combined proportion of the poor and fair classes was projected to decrease by 3.04 percentage points.

5 Discussion

5.1 Propagation of Terrain-Induced Errors in MRSEI

EEQ assessments in complex plateau–mountain regions are more strongly affected by topographic relief and illumination conditions[58]. Because slope, aspect, and solar incidence angle vary substantially across mountainous terrain, the same land-cover type may exhibit different surface reflectance characteristics on illuminated and shaded slopes[18]. Ecological indices derived from uncorrected optical bands may reflect not only the actual surface ecological conditions but also radiometric differences caused by mountain shadows, aspect-related illumination differences, and local topographic relief, as illustrated in Figure 9a and c. Such interference from nonecological factors can exaggerate apparent differences in ecological quality among slope aspects, thereby reducing the accuracy of EEQ assessments in plateau–mountain regions (Figure 9b and d).

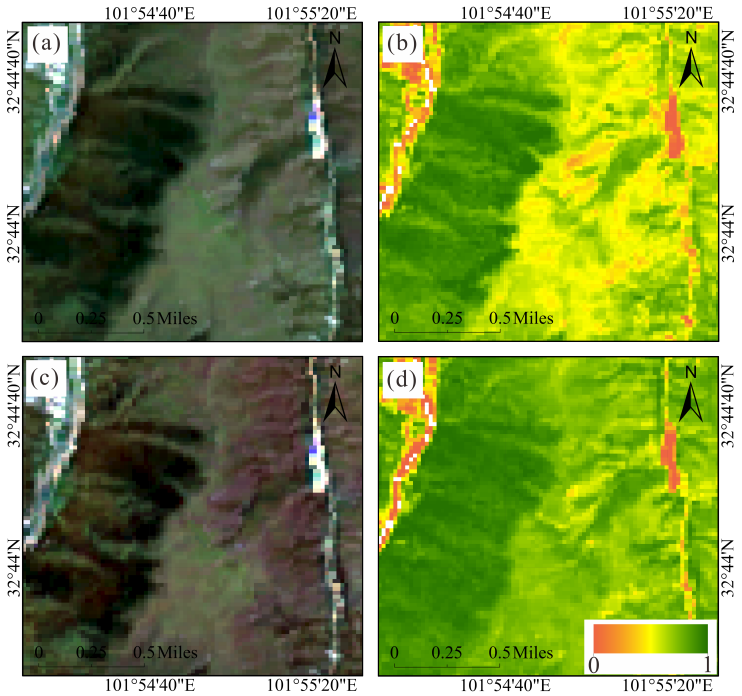


Fig. 9. Comparison of remote sensing imagery (2025) and MRSEI before and after topographic correction. (**a**) Remote sensing imagery without topographic correction. (**b**) MRSEI without topographic correction. (**c**) Remote sensing imagery after SCS+C topographic correction. (**d**) MRSEI after SCS+C topographic correction.

SCS+C correction reduced the dependence of spectral bands on terrain illumination, thereby weakening the propagation of terrain-induced radiometric differences into MRSEI (Figure 3). The grouped statistical results based on the cosine of the solar incidence angle ($\cos i$) indicate that when $\cos i$ is less than 0.6, corresponding to a solar incidence angle greater than 53°, the mean uncorrected MRSEI is generally higher than the corrected mean (Figure 10a). The two values gradually converged when $\cos i$ ranged from 0.6 to 0.8. When $\cos i > 0.8$, improved slope illumination and weakened terrain-shadow effects resulted in the corrected MRSEI being slightly higher than the uncorrected value (Figure 10a). This indicates that SCS+C does not adjust all pixels in the same direction; rather, it modifies the spectral reflectance of different terrain units according to their illumination conditions.

A further comparison between the high-illumination ($\cos i > 0.8$) and low-illumination ($\cos i < 0.6$) groups showed that the correction increased the median MRSEI of the high-illumination group from 0.611 to 0.649, while decreasing that of the low-illumination group from 0.771 to 0.727. Consequently, the difference in median MRSEI between the two groups decreased from 0.160 to 0.078 (Figure 10b). The comparison before and after correction indicates that differences in MRSEI among illumination conditions were partly amplified by terrain-induced radiometric effects, whereas SCS+C reduced the nonecological contrast associated with terrain illumination. Notably, the median MRSEI of the low-illumination group remained higher than that of the high-illumination group after correction. Therefore, differences among slope aspects cannot be attributed entirely to observational errors associated with solar incidence angle and terrain shadows, but may also reflect the combined effects of land-cover composition, local hydrothermal conditions, topographic position, and residual correction errors.

Improving the vegetation-index component was intended to alleviate the asymptotic saturation of conventional NDVI and its reduced sensitivity to canopy variation under high-biomass conditions. By applying a nonlinear kernel transformation to the relationship between the red and near-infrared bands, kNDVI adaptively stretches the index dynamic range and exploits higher-order spectral relations, thereby enhancing sensitivity to vegetation biophysical and physiological variability and subtle greenness differences in densely vegetated areas.

Using spatially matched vegetation-index and land-cover pixels, the calculated results showed that the within-class standard deviations of the NDVI-based MRSEI were approximately 0.038, 0.029, and 0.074 for forest, shrubland, and grassland, respectively. After NDVI was replaced with kNDVI, the corresponding standard deviations increased to approximately 0.100, 0.084, and 0.187 (Figure 11a). Meanwhile, the median NDVI-MRSEI values for these vegetation types were concentrated within a relatively narrow range of 0.864–0.905, whereas the median kNDVI-MRSEI values ranged from 0.678 to 0.787 and exhibited wider interquartile ranges and overall distributions (Figure 11b). Different vegetation indices have distinct value ranges, and direct comparisons of their numerical values may therefore lead to interpretive bias. Subsequent normalization may also be affected by the data distribution and extreme values.

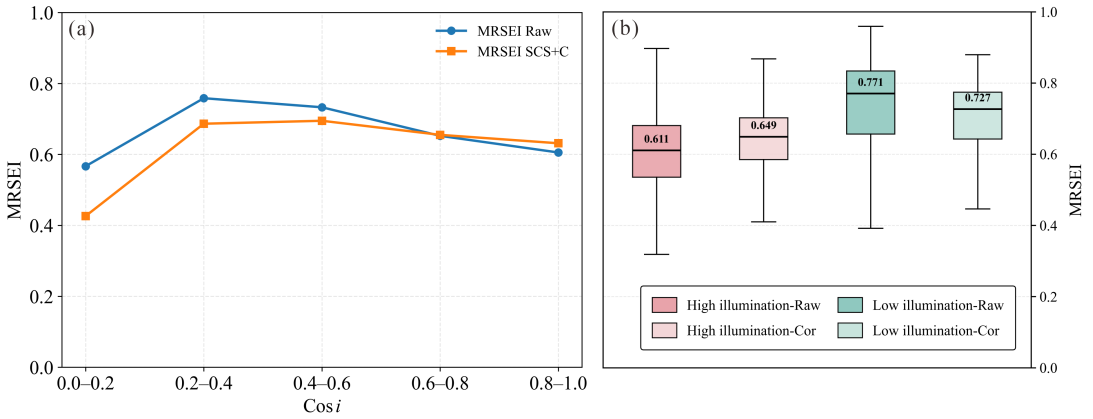


Fig. 10. Effects of SCS+C topographic correction. (**a**) Comparison of mean MRSEI before and after SCS+C topographic correction. (**b**) Comparison of MRSEI distributions in the low-illumination ($\cos i < 0.6$) and high-illumination ($\cos i > 0.8$) groups before and after SCS+C topographic correction.

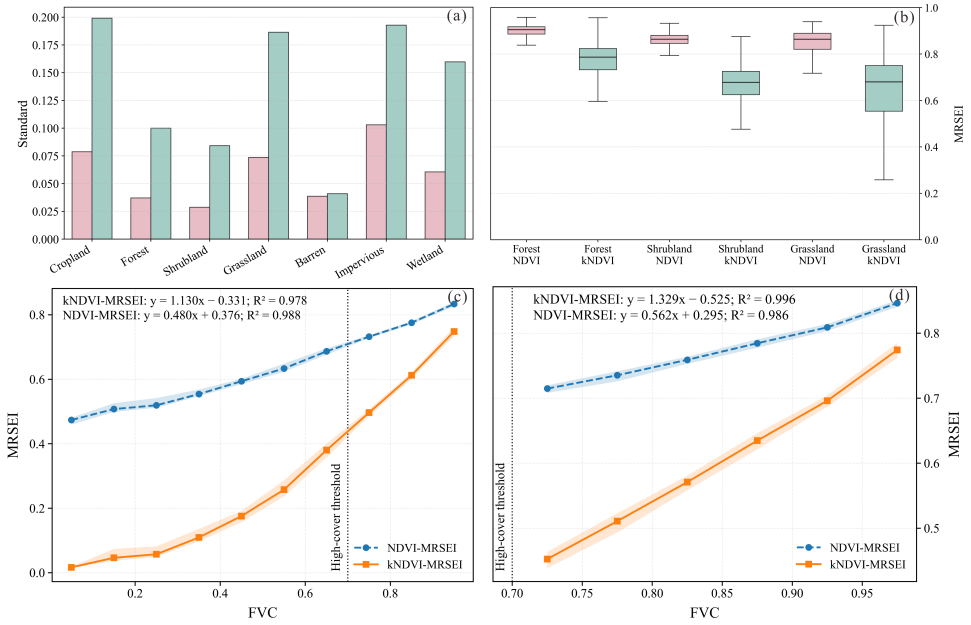


Fig. 11. Comparison of the ability of NDVI-based MRSEI and kNDVI-based MRSEI to differentiate among land-cover types. (**a**) Comparison of within-class standard deviations between NDVI-based MRSEI and kNDVI-based MRSEI across different land-cover types. (**b**) Differences in the distributions of NDVI-based MRSEI and kNDVI-based MRSEI within densely vegetated land-cover types, including forest, shrubland, and grassland. (**c**) Correlations of NDVI-MRSEI and kNDVI-MRSEI with FVC. (**d**) Correlations of NDVI-MRSEI and kNDVI-MRSEI with FVC in high-vegetation-cover areas.

Consequently, the lower median MRSEI value does not necessarily indicate an overall deterioration in regional ecological quality; instead, it may largely reflect the rescaling of the value distribution caused by the nonlinear transformation of kNDVI and subsequent normalization[59,60]. The increased within-class dispersion indicates that the previous concentration of high values was reduced, enabling MRSEI to more effectively differentiate ecological conditions within the same vegetation type.

Fractional vegetation cover (FVC) was further used to evaluate this improvement in sensitivity. Across the full range of land cover, the regression slope between kNDVI-MRSEI and FVC was 1.13, substantially higher than the corresponding slope of 0.48 for NDVI-MRSEI (Figure 11c). In densely vegetated areas with FVC > 0.7, the respective slopes were 1.32 and 0.562 (Figure 11d). The steeper slopes indicate that kNDVI-MRSEI was more responsive to changes in land cover and retained more subtle variation, particularly in high-cover areas where conventional NDVI is prone to saturation. Together with the correlation-based validation against NPP and EVI, these findings suggest that incorporating kNDVI improves the capacity of the composite ecological index to represent vegetation productivity, vegetation-cover conditions, and ecological variation within densely vegetated areas.

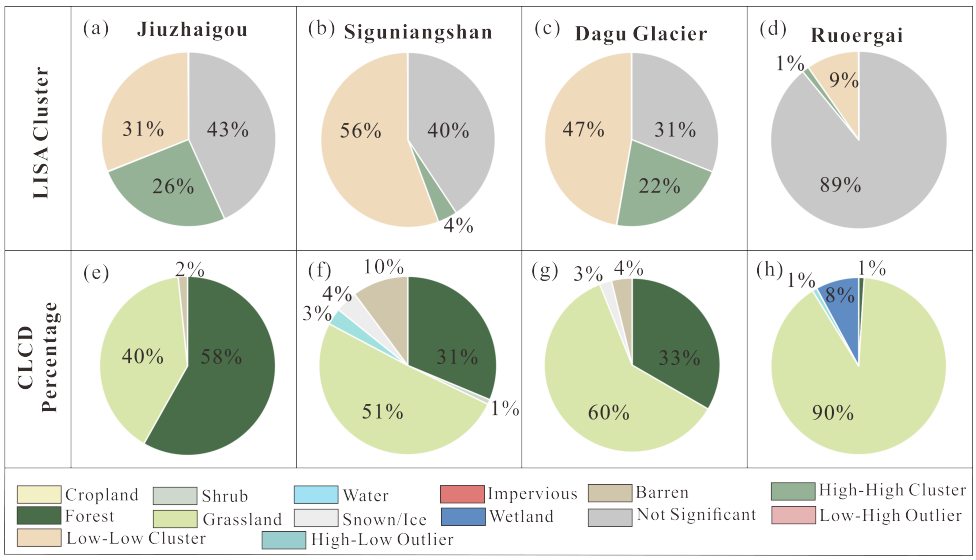


Fig. 12. LISA cluster composition of MRSEI and land-cover structure in representative nature reserves of Aba Prefecture. (**a**) Composition of LISA cluster types in Jiuzhaigou Nature Reserve. (**b**) Composition of LISA cluster types in Siguniangshan Nature Reserve. (**c**) Composition of LISA cluster types in Dagu Glacier Nature Reserve. (**d**) Composition of LISA cluster types in Ruoergai Nature Reserve. (**e**) Land-cover composition of LISA cluster types in Jiuzhaigou Nature Reserve. (**f**) Land-cover composition of LISA cluster types in Siguniangshan Nature Reserve. (**g**) Land-cover composition of LISA cluster types in Dagu Glacier Nature Reserve. (**h**) Land-cover composition of LISA cluster types in Ruoergai Nature Reserve.

5.2 Spatiotemporal Heterogeneity of Ecological Quality and Its Ecological Interpretation

The complex topographic structure and pronounced environmental gradients of Aba Prefecture jointly shaped the spatiotemporal heterogeneity of ecological quality. Although regional ecological quality generally improved, it exhibited substantial interannual variability, and MRSEI showed no stable linear relationship with any single climatic or anthropogenic factor. In contrast, land cover had the largest single model-attributed contribution and directly represented surface ecological conditions, providing a basis for interpreting differences in the spatial clustering patterns of ecological quality.

The spatial autocorrelation analysis of ecological quality in Aba Prefecture revealed a strong positive spatial association (Figure 6). High–high clusters were mainly distributed in the well-vegetated mountainous areas of the eastern and southeastern regions, whereas low–low clusters occurred primarily in ecologically constrained areas, such as high-elevation barren land, mountain ridges, and the margins of snow- and ice-covered areas. The clustering patterns of the individual nature reserves further revealed this spatial heterogeneity (Figure 12). Jiuzhaigou Nature Reserve spans an elevation range of 1997–4846 m, with forest and grassland accounting for 58% and 40% of its area, respectively. The continuous forest and grassland cover provides a basis for the aggregation of high ecological quality, resulting in high–high clusters accounting for 26% of the reserve. However, mountain altitudinal zonation and localized high-elevation environments also contributed to low–low clusters, which accounted for 31% (Figure 12a and e). Compared with Jiuzhaigou Nature Reserve, Siguniangshan Nature Reserve has a higher elevation range of 2896–5973 m. Although grassland and forest still account for 51% and 31% of its area, respectively, barren land and snow and ice comprise 10% and 4%. The alpine environment and extensive exposed surfaces impose substantial constraints on ecological quality, resulting in low–low clusters increasing to 56%, whereas high–high clusters account for only 4% (Figure 12b and f). Similarly, Dagu Glacier Nature Reserve contains appreciable proportions of barren land and snow and ice. The reserve spans an elevation range of 2401–5150 m, with grassland and forest accounting for 60% and 33% of its area, respectively. Its spatial pattern is characterized by the coexistence of high- and low-value clusters, with high–high clusters accounting for 22% and low–low clusters for 47% (Figure 12c and g). Ruoergai Nature Reserve exhibited a different pattern. Its elevation is concentrated within a relatively narrow range of 3307–3710 m, and the terrain is comparatively gentle. Grassland and wetland account for 90% and 8% of the reserve, respectively. The continuous and relatively homogeneous grassland–wetland landscape resulted in weak local clustering of high and low values, with nonsignificant areas accounting for 89% (Figure 12d and h). Therefore, areas with greater forest cover and relatively favorable elevation conditions are more likely to form high-value MRSEI clusters, whereas high-elevation areas dominated by barren land, snow, and ice are more prone to low-value clustering. In contrast, areas with continuous grassland–wetland cover predominantly exhibit spatial homogeneity.

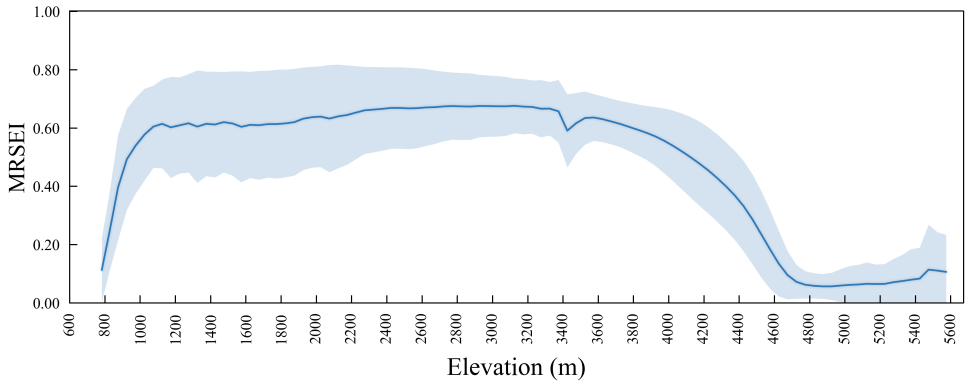


Fig. 13. Variation in MRSEI along the elevation gradient.

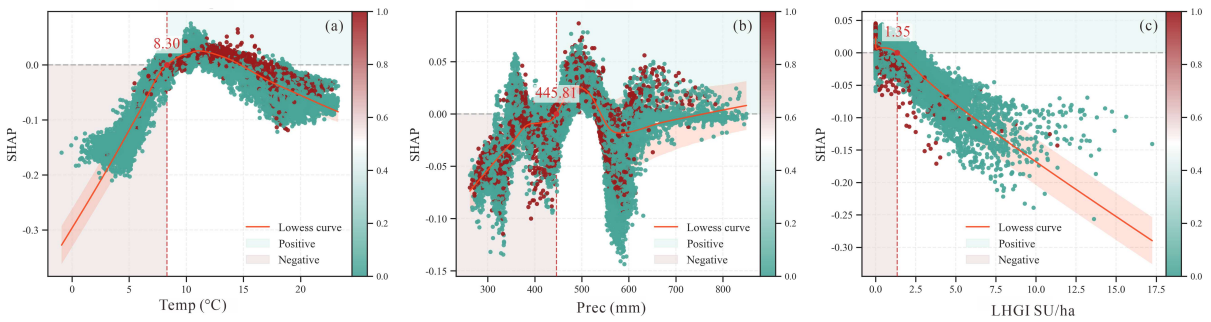


Fig. 14. SHAP dependence relationships and threshold effects of air temperature, precipitation, and grazing intensity on MRSEI. (**a**) SHAP dependence relationship and threshold effect of air temperature on MRSEI. (**b**) SHAP dependence relationship and threshold effect of precipitation on MRSEI. (**c**) SHAP dependence relationship and threshold effect of grazing intensity on MRSEI.

5.3 Coupled Effects of Climate Change and Human Activities on MRSEI

The spatiotemporal variations in ecological quality across Aba Prefecture were jointly influenced by plateau topography, climate, land cover, and human activities. The SHAP results showed that topographic and climatic factors constituted the primary natural geographic constraints on ecological quality in the plateau–mountain environment, with a combined contribution of 58.7% (Figure 7). Among the topographic factors, elevation, represented by the DEM, exerted the dominant influence, contributing 19.1% (Figure 7).

MRSEI exhibited a pronounced nonlinear pattern along the elevation gradient. Ecological quality in low-elevation areas generally remained below the good level. As elevation increased, MRSEI rose rapidly, reaching approximately 0.6 at an elevation of around 1100 m (Figure 13). Across the study area, MRSEI generally remained at a relatively high level within the low- to middle-elevation range of approximately 1100–3800 m, which corresponds mainly to the forested areas in the eastern and southeastern regions and the Ruoergai wetland area in the north. At higher elevations, however, MRSEI began to decline markedly, with the rate of decrease becoming greater above 3800 m in the western and southwestern parts of the study area. Natural constraints associated with high elevations, including low temperatures, short growing seasons, and increased snow cover, jointly limited further improvements in ecological quality.

Conditioned by the underlying topographic setting, the effects of temperature and precipitation on MRSEI exhibited distinct optimal ranges and stage-dependent responses[61,62]. At lower temperatures, MRSEI generally exhibited a negative response, indicating that cold conditions substantially constrained vegetation growth and ecological improvement. Once temperature exceeded approximately 8.30 °C, its effect gradually shifted from negative to positive, suggesting that moderate warming improved conditions for vegetation growth (Figure 14a). Once air temperature exceeds a certain range, continued warming enhances evapotranspiration and atmospheric water demand, reduces ecosystem water availability, and further constrains vegetation growth and improvements in ecological quality. Consequently, the SHAP value gradually declines, indicating a weakening marginal contribution of air temperature to MRSEI[63,64]. The response to precipitation also exhibited a clear threshold effect. Moderate precipitation promoted vegetation growth and improved surface moisture conditions (Figure 14b), whereas the positive response of MRSEI weakened under either insufficient or anomalously high precipitation. These findings indicate that plateau–mountain ecosystems are highly sensitive to hydrothermal conditions.

Aba Prefecture is predominantly mountainous, with relatively limited urbanization and expansion of built-up land. Consequently, urbanization indicators such as nighttime light intensity contributed relatively little to ecological quality at the regional scale, and the effects of human activities on MRSEI exhibited pronounced spatial heterogeneity. In contrast, grazing intensity more directly reflects anthropogenic pressure on plateau grassland and wetland ecosystems. At relatively low grazing intensities, its effect on MRSEI was limited. As LHGI increased, however, overgrazing reduced grassland cover, promoted the expansion of barren land, and weakened soil conservation and ecological recovery capacity. These effects were particularly pronounced in ecologically sensitive areas, such as alpine grasslands and wetland margins, thereby further increasing the risk of ecological quality degradation (Figure 14c). Therefore, the influence of human activities on MRSEI in Aba Prefecture was not dominated by urban expansion, but was primarily manifested through the persistent disturbance of local ecosystems associated with grassland-use intensity.

6 Conclusions

Ecological quality assessment in plateau–mountain regions needs to account for both terrain-induced radiometric effects and the regional applicability of ecological indicators. Based on Landsat observations from 1996 to 2025, this study developed an MRSEI framework for complex plateau–mountain environments by integrating scene-specific SCS+C topographic correction, kNDVI, and ecological-direction-constrained PCA reconstruction. The SCS+C correction substantially reduced the dependence of apparent reflectance in the red and near-infrared bands on solar incidence geometry. MRSEI also showed greater consistency with NPP, EVI, and LHGI than the conventional RSEI.

From 1996 to 2025, MRSEI exhibited pronounced interannual fluctuations but maintained an overall upward trend. The multiyear mean MRSEI showed strong positive spatial autocorrelation (Moran's I = 0.89), with high–high clusters concentrated mainly in the forested mountainous areas of the eastern and southeastern parts of the study area. The XGBoost model achieved an R^2 of 0.44 in the temporally independent holdout validation. Topographic, climatic, land-cover, and human-activity variables accounted for 30.9%, 27.8%, 23.9%, and 17.4% of the total mean absolute SHAP importance, respectively. Under the natural development scenario, the regional mean MRSEI is projected to decrease from 0.6596 in 2024 to 0.6472 in 2034. The proportion of the area classified as excellent is projected to decrease by 5.70 percentage points, whereas the proportions classified as moderate and good are projected to increase by 5.25 and 3.49 percentage points, respectively. These findings provide a methodological reference for long-term ecological monitoring and spatially targeted restoration in plateau–mountain regions.

Data Availability. All datasets used in this study are publicly available from the sources listed in Table 1, where the corresponding access links are provided.

References

1. Tefera, G. W., Ray, R. L. & Bantider, A. Exploring the unique biophysical characteristics and ecosystem services of mountains: A review. *J. Mt. Sci.* **21**, 3584–3597 (2024).
2. Xue, J., Li, Z., Feng, Q., Gui, J. & Zhang, B. Spatiotemporal variations of water conservation and its influencing factors in ecological barrier region, Qinghai-Tibet Plateau. *J. Hydrol. Reg. Stud.* **42**, 101164 (2022).
3. Sundqvist, M. K., Sanders, N. J. & Wardle, D. A. Community and Ecosystem Responses to Elevational Gradients: Processes, Mechanisms, and Insights for Global Change. *Annu. Rev. Ecol. Evol. Syst.* **44**, 261–280 (2013).
4. Wu, Y. *et al.* Elevation-Dependent Contribution of the Response and Sensitivity of Vegetation Greenness to Hydrothermal Conditions on the Grasslands of Tibet Plateau from 2000 to 2021. *Remote Sens.* **16**, 201 (2024).
5. Li, C. *et al.* Evaluating the impact of highway construction projects on landscape ecological risks in high altitude plateaus. *Sci. Rep.* **12**, 5170 (2022).
6. Pettorelli, N. *et al.* Satellite remote sensing for applied ecologists: opportunities and challenges. *J. Appl. Ecol.* **51**, 839–848 (2014).
7. Tucker, C. J. Red and photographic infrared linear combinations for monitoring vegetation. *Remote Sens. Environ.* **8**, 127–150 (1979).

8. Huete, A. *et al.* Overview of the radiometric and biophysical performance of the MODIS vegetation indices. *Remote Sens. Environ.* **83**, 195–213 (2002).

9. Liu, Y., Xiang, W., Hu, P., Gao, P. & Zhang, A. Evaluation of Ecological Environment Quality Using an Improved Remote Sensing Ecological Index Model. *Remote Sens.* **16**, 3485 (2024).

10. Xu, H. A remote sensing index for assessment of regional ecological changes. *China Environ. Sci.* **33**, 889–897 (2013).

11. Zhang, W., Zhang, W., Ji, J. & Chen, C. Urban Ecological Quality Assessment Based on Google Earth Engine and Driving Factors Analysis: A Case Study of Wuhan City, China. *Sustainability* **16**, 3598 (2024).

12. Zhang, L., Hou, Q., Duan, Y. & Ma, S. Spatial and Temporal Heterogeneity of Eco-Environmental Quality in Yanhe Watershed (China) Using the Remote-Sensing-Based Ecological Index (RSEI). *Land* **13**, 780 (2024).

13. Peng, X. *et al.* Unraveling the Ecological Tapestry: A Comprehensive Assessment of Changtang Nature Reserve's Ecological and Environmental Using RSEI and GEE. *Land* **12**, 1581 (2023).

14. Xi, R. *et al.* Spatiotemporal dynamic and drivers of ecological environmental quality on the Chinese Loess Plateau: Insights from kRSEI model and climate-human interaction analysis. *J. Arid Land* **17**, 958–978 (2025).

15. Gorelick, N. *et al.* Google Earth Engine: Planetary-scale geospatial analysis for everyone. *Remote Sens. Environ.* **202**, 18–27 (2017).

16. Wulder, M. A. *et al.* Current status of Landsat program, science, and applications. *Remote Sens. Environ.* **225**, 127–147 (2019).

17. Chen, R. *et al.* Topographic Correction of Optical Remote Sensing Images in Mountainous Areas: A systematic review. *IEEE Geosci. Remote Sens. Mag.* **11**, 125–145 (2023).

18. Li, A., Wang, Q., Bian, J. & Lei, G. An Improved Physics-Based Model for Topographic Correction of Landsat TM Images. *Remote Sens.* **7**, 6296–6319 (2015).

19. Vázquez-Jiménez, R., Romero-Calcerrada, R., Ramos-Bernal, R., Arrogante-Funes, P. & Novillo, C. Topographic Correction to Landsat Imagery through Slope Classification by Applying the SCS + C Method in Mountainous Forest Areas. *ISPRS Int. J. Geo-Inf.* **6**, 287 (2017).

20. Nie, X., Hu, Z., Zhu, Q. & Ruan, M. Research on Temporal and Spatial Resolution and the Driving Forces of Ecological Environment Quality in Coal Mining Areas Considering Topographic Correction. *Remote Sens.* **13**, 2815 (2021).

21. Gitelson, A. A. Wide Dynamic Range Vegetation Index for Remote Quantification of Biophysical Characteristics of Vegetation. *J. Plant Physiol.* **161**, 165–173 (2004).

22. Camps-Valls, G. *et al.* A unified vegetation index for quantifying the terrestrial biosphere. *Sci. Adv.* **7**, eabc7447 (2021).

23. Jolliffe, I. T. & Cadima, J. Principal component analysis: a review and recent developments. *Philos. Trans. R. Soc. A Math. Phys. Eng. Sci.* **374**, 20150202 (2016).

24. Liu, P., Ren, C., Yu, W., Ren, H. & Xia, C. Exploring the ecological quality and its drivers based on annual remote sensing ecological index and multisource data in Northeast China. *Ecol. Indic.* **154**, 110589 (2023).

25. Elith, J., Leathwick, J. R. & Hastie, T. A working guide to boosted regression trees. *J. Anim. Ecol.* **77**, 802–813 (2008).

26. Xia, J., Zhang, G., Ma, S. & Pan, Y. Spatial Heterogeneity of Driving Factors in Multi-Vegetation Indices RSEI Based on the XGBoost-SHAP Model: A Case Study of the Jinsha River Basin, Yunnan. *Land* **14**, 925 (2025).

27. Chen, T. & Guestrin, C. XGBoost: A Scalable Tree Boosting System. In Proceedings of the 22nd ACM SIGKDD International Conference on Knowledge Discovery and Data Mining, pp. 785–794, ACM (2016).

28. Lundberg, S. M. & Lee, S.-I. A Unified Approach to Interpreting Model Predictions. In Advances in Neural Information Processing Systems 30, pp. 4765–4774, Curran Associates, Inc. (2017).

29. Chen, Y., Ning, X., Zhang, H., Lan, X. & Chang, Z. Remote sensing ecological index (RSEI) model and its applications: A review. *Remote Sens. Nat. Resour.* **36**, 28–40 (2024).

30. Lv, Y., Xiu, L., Yao, X., Yu, Z. & Huang, X. Spatiotemporal evolution and driving factors analysis of the eco-quality in the Lanxi urban agglomeration. *Ecol. Indic.* **156**, 111114 (2023).

31. Chen, W. *et al.* Detecting Long-Term Series Eco-Environmental Quality Changes and Driving Factors Using the Remote Sensing Ecological Index with Salinity Adaptability ($RSEI_{SI}$): A Case Study in the Tarim River Basin, China. *Land* **12**, 1309 (2023).

32. Liu, P., Wen, T., Han, R. & Wu, S. Study on RSEI Changes Using Remote Sensing and Markov-FLUS Modeling Approach. *Sustainability* **17**, 10267 (2025).

33. Prestele, R. *et al.* Hotspots of uncertainty in land-use and land-cover change projections: a global-scale model comparison. *Glob. Change Biol.* **22**, 3967–3983 (2016).

34. You, C., Qu, H., Zhang, S. & Guo, L. Assessment of Uncertainties in Ecological Risk Based on the Prediction of Land Use Change and Ecosystem Service Evolution. *Land* **13**, 535 (2024).

35. Wang, C., Zhang, S. & Guo, L. Environmental Sensitivity Evaluation of Aba Tibetan and Qiang Autonomous Prefecture Based on GIS and RS. *E3S Web Conf.* **406**, 04026 (2023).

36. Huang, L., Xiao, J., Zhou, Z. & Ren, P. Study on the Evolution of the Mountain Ecological Environment Based on Remote Sensing and Water Footprints: Case Study of Northwestern Sichuan, Southwest China. *Remote Sens.* **16**, 4412 (2024).

37. Veeck, G. Grassland protection policy in China: Post-Wenchuan economic and environmental change in Aba prefecture, Sichuan Province. *Environ. Sci. Policy* **139**, 195–203 (2023).

38. Yang, X. *et al.* Socio-Ecological Vulnerability in Aba Prefecture, Western Sichuan Plateau: Evaluation, Driving Forces and Scenario Simulation. *ISPRS Int. J. Geo-Inf.* **11**, 524 (2022).

39. Deng, G. *et al.* Understanding human and nature interaction outcomes for sustaining tourist destinations: An example of Jiuzhaigou Nature Reserve, China. *Aquat. Ecosyst. Health Manag.* **23**, 373–384 (2020).

40. Pekel, J.-F., Cottam, A., Gorelick, N. & Belward, A. S. High-resolution mapping of global surface water and its long-term changes. *Nature* **540**, 418–422 (2016).

41. Teillet, P., Guindon, B. & Goodenough, D. On the Slope-Aspect Correction of Multispectral Scanner Data. *Can. J. Remote Sens.* **8**, 84–106 (1982).

42. Soenen, S., Peddle, D. & Coburn, C. SCS+C: a modified Sun-canopy-sensor topographic correction in forested terrain. *IEEE Trans. Geosci. Remote Sens.* **43**, 2148–2159 (2005).

43. Rouse, J. W., Jr., Haas, R. H., Schell, J. A. & Deering, D. W. Monitoring Vegetation Systems in the Great Plains with ERTS. Conference Paper NASA SP-351, NASA Goddard Space Flight Center, Washington, DC, USA (1974). Proceedings of the Third Earth Resources Technology Satellite-1 Symposium, Vol. 1, pp. 309–317.

44. Crist, E. P. A TM Tasseled Cap equivalent transformation for reflectance factor data. *Remote Sens. Environ.* **17**, 301–306 (1985).

45. Huang, C., Wylie, B., Yang, L., Homer, C. & Zylstra, G. Derivation of a tasselled cap transformation based on Landsat 7 at-satellite reflectance. *Int. J. Remote Sens.* **23**, 1741–1748 (2002).

46. Baig, M. H. A., Zhang, L., Shuai, T. & Tong, Q. Derivation of a tasselled cap transformation based on Landsat 8 at-satellite reflectance. *Remote Sens. Lett.* **5**, 423–431 (2014).

47. Malakar, N. K. *et al.* An Operational Land Surface Temperature Product for Landsat Thermal Data: Methodology and Validation. *IEEE Trans. Geosci. Remote Sens.* **56**, 5717–5735 (2018).

48. U.S. Geological Survey. Landsat Collection 2 Level-2 Science Products. Tech. Rep. Fact Sheet 2021-3055, U.S. Geological Survey (2021).

49. Rikimaru, A., Roy, P. S. & Miyatake, S. Tropical Forest Cover Density Mapping. *Trop. Ecol.* **43**, 39–47 (2002).

50. Xu, H. A new index for delineating built-up land features in satellite imagery. *Int. J. Remote Sens.* **29**, 4269–4276 (2008).

51. Zheng, Z., Wu, Z., Chen, Y., Guo, C. & Marinello, F. Instability of remote sensing based ecological index (RSEI) and its improvement for time series analysis. *Sci. Total Environ.* **814**, 152595 (2022).

52. Ning, L., Wang, J. & Qin, F. The improvement of ecological environment index model RSEI. *Arab. J. Geosci.* **13**, 403 (2020).

53. Xu, M. *et al.* An improved estimation of remote sensing-based ecological index for tracking continuous changes in eco-environmental quality. *Int. J. Digit. Earth* **17**, 2445625 (2024).

54. Moran, P. A. P. Notes on Continuous Stochastic Phenomena. *Biometrika* **37**, 17–23 (1950).

55. Anselin, L. Local Indicators of Spatial Association—LISA. *Geogr. Anal.* **27**, 93–115 (1995).

56. Lundberg, S. M. *et al.* From local explanations to global understanding with explainable AI for trees. *Nat. Mach. Intell.* **2**, 56–67 (2020).

57. Liang, X. *et al.* Understanding the drivers of sustainable land expansion using a patch-generating land use simulation (PLUS) model: A case study in Wuhan, China. *Comput. Environ. Urban Syst.* **85**, 101569 (2021).

58. Chen, R., Yin, G., Liu, G., Li, J. & Verger, A. Evaluation and normalization of topographic effects on vegetation indices. *Remote Sensing* **12**, 2290 (2020).

59. Franquesa, M., Adell-Michavila, M. & Vicente-Serrano, S. M. Long-term vegetation dynamics in Spain's national park network: Insights from remote sensing data. *Environ. Monit. and Assess.* **197**, 767 (2025).

60. Guo, L., Xu, C., Wu, H., Shi, M. & Fan, Y. The decisive influence of the improved remote sensing ecological index on the terrestrial ecosystem in typical arid areas of China. *Land* **13**, 2162 (2024).

61. Wang, Y. *et al.* Contrasting effects of temperature and precipitation on vegetation greenness along elevation gradients of the Tibetan Plateau. *Remote Sens.* **12**, 2751 (2020).

62. Qiao, B. *et al.* Nonlinear threshold effects of environmental drivers on vegetation cover in mountain ecosystems: From constraint mechanisms to adaptive management. *Ecol. Indic.* **173**, 113328 (2025).

63. Dai, X., Yu, Z., Matheny, A. M., Zhou, W. & Xia, J. Increasing evapotranspiration decouples the positive correlation between vegetation cover and warming in the tibetan plateau. *Front. in Plant Sci.* **13**, 974745 (2022).

64. Yuan, W. *et al.* Increased atmospheric vapor pressure deficit reduces global vegetation growth. *Sci. Adv.* **5**, eaax1396 (2019).

Funding. This research was supported by the Natural Science Foundation of Sichuan Province (Grant No. 2025NSFSC2089), the Central Government-Guided Local Science and Technology Development Program of Sichuan Province (Grant No. 2025ZYD0082), the Aba Prefecture Science and Technology Achievement Transformation Program (Grant No. R25CGZH0005), and the Open Research Fund of the Fujian Key Laboratory of Severe Weather and the Key Laboratory of Straits Severe Weather, China Meteorological Administration (Grant No. 2024KFKT07).

Author contributions. Conceptualization, S.H. and J.L.; methodology, S.H. and X.Q.; validation, S.N. and S.H.; formal analysis, S.H. and X.Q.; investigation, S.H., S.N., S.Z. and J.L.; data curation, S.H. and S.N.; resources, S.Z. and J.L.; writing—original draft preparation, S.H.; writing—review and editing, J.L. and X.Q.; supervision, S.Z. and J.L.; funding acquisition, S.Z. and J.L. All authors have read and approved the submitted version of the manuscript.

Competing interests. The authors declare no competing interests.